Nanoscale spectroscopy with polarized X-rays by NEXAFS-TXM

Peter Guttmann, Carla Bittencourt, Stefan Rehbein, Polona Umek, Xiaoxing Ke, Gustaaf van Tendeloo, Christopher Ewels, Gerd Schneider

Nanoscale spectroscopy with polarized X-rays by NEXAFS-TXM

Peter Guttmann[1], Carla Bittencourt[2]*, Stefan Rehbein[1], Polona Umek[3], Xiaoxing Ke[2], Gustaf Van Tendeloo[2], Chris P. Ewels[4] and Gerd Schneider[1]*

Near-edge X-ray absorption spectroscopy (NEXAFS)[1] is an essential analytical tool in material science. Combining NEXAFS with scanning transmission X-ray microscopy (STXM) adds spatial resolution and the possibility to study individual nanostructures[2,3]. Here, we describe a full-field transmission X-ray microscope (TXM) that generates high-resolution, large-area NEXAFS data with a collection rate two orders of magnitude faster than is possible with STXM. The TXM optical design combines a spectral resolution of $E/\Delta E = 1 \times 10^4$ with a spatial resolution of 25 nm in a field of view of 15–20 μm and a data acquisition time of ∼1 s. As an example, we present image stacks and polarization-dependent NEXAFS spectra from individual anisotropic sodium and protonated titanate nanoribbons. Our NEXAFS-TXM technique has the advantage that one image stack visualizes a large number of nanostructures and therefore already contains statistical information. This new high-resolution NEXAFS-TXM technique opens the way to advanced nanoscale science studies.

The electronic structure of single individual nanostructures cannot be studied with conventional non-spatially resolved techniques such as X-ray absorption spectroscopy or photoelectron spectroscopy. These spectroscopy techniques typically illuminate areas of $50 \times 50\ \mu m^2$ or larger. Consequently, the electronic structure information is averaged over many individual nanostructures. In contrast, techniques based on spectromicroscopy, such as electron energy loss spectroscopy (EELS), performed in monochromated, aberration-corrected transmission electron microscopes operating at low voltages, permit spectroscopy in isolated electron-beam-sensitive nanostructures with an energy resolution comparable to synchrotron-based spectrometry methods. However, such techniques are limited to a sample thickness of a few atomic diameters[4–6]. Furthermore, measurements of the polarization dependence (linear dichroism) via the momentum transfer directional dependence are much less convenient in an electron microscope than polarization-dependent measurements using synchrotron sources[7]. In this context, X-ray spectroscopy methods can probe the electronic structure as a function of the orientation of the E-vector of the linearly polarized X-rays relative to a characteristic direction of an anisotropic sample. This provides information on spectral assignments, molecular orientation or degree of alignment in the sample[8,9].

The combination of X-ray absorption spectroscopy and high spatial resolution opens the way to studying the electronic structure of isolated nanostructures with nanoscale spatial resolution. Until now, spectroscopic analysis with nanometre resolution was essentially restricted to X-ray photoemission electron microscopy (XPEEM)[10], scanning transmission X-ray microscopy (STXM)[3,11] and EELS microscopy[12,13]. Both STXM and EELS microscopy use image fields containing only one or a few nanostructures, and therefore do not deliver statistical information. In the STXM, the image is formed by raster-scanning the focal spot of the objective relative to the sample and detecting locally the transmitted X-ray photons[11]. Given this process of sequential image formation and the limitation that only a small fraction of the spatially coherent undulator photon flux can be used, image formation is relatively slow and favours small fields of view in the range of a few micrometres. As the image is formed pixel by pixel, the contrast transfer function (CTF) basically follows that of an incoherent microscope. The radiation dose required to detect small object features is proportional to $(C_{obj} \times CTF)^{-2}$ where C_{obj} denotes the object contrast[14]. Therefore, microscopes that provide a high contrast transfer are advantageous in that sample damage and exposure time are minimized. There is also a reduction in the occurrence of artefacts in the measured absorption values from the original object contrast for higher spatial frequencies. Compared to STXMs[3,11], our new transmission X-ray microscope (TXM) operates under partially coherent conditions that yield a high contrast transfer[15]. However, the radiation dose applied in an STXM may be lower, because, unlike a TXM, there is no objective between the sample and detector.

Here, we report the first demonstration of near-edge X-ray absorption spectroscopy (NEXAFS) in a full-field TXM. Previous generations of TXM provided only a low spectral resolution ($E/\Delta E \leq 500$), which excludes NEXAFS measurements[1]. Our TXM uses an undulator X-ray source and a focusing spherical grating monochromator (FSGM) to generate the required high spectral resolution of $E/\Delta E = 1 \times 10^4$. A single reflection ellipsoidal mirror condenser with 80% focusing efficiency is used for the illumination of an object field with a diameter of 15–20 μm, which is large compared to the size of individual nanostructures. For the present study, a zone plate objective with an outermost zone width of 40 nm was used to image the sample onto a cooled back-illuminated soft X-ray charge-coupled device (CCD) camera (Roper Scientific, PI SX1300).

During NEXAFS image data acquisition, only the objective has to be moved, because the reflective condenser works largely independently of the photon energy. For different photon energies the slight changes in magnification are corrected by relocating the CCD camera. Note that the TXM is not restricted to the small fraction of spatially coherent photon flux from the undulator, and the field of view is imaged simultaneously onto the CCD camera[15]. Therefore, the data acquisition time for larger fields of view is at least two orders of magnitude faster in the TXM than in an

[1]Helmholtz-Zentrum für Materialien und Energie GmbH, Institute for Soft Matter and Functional Materials, Albert-Einstein-Str. 15, 12489 Berlin, Germany, [2]Electron Microscopy for Materials Science, University of Antwerp, Groenenborgerlaan 171, 2020 Antwerp, Belgium, [3]Jožef Stefan Institute, Jamova 39, 1000 Ljubljana, Slovenia, [4]CNRS UMR6502, Institut des Matériaux Jean Rouxel, Université de Nantes, rue de la Houssiniere 2, 44322 Nantes, France.
*e-mail: carla.bittencourt@ua.ac.be; gerd.schneider@helmholtz-berlin.de

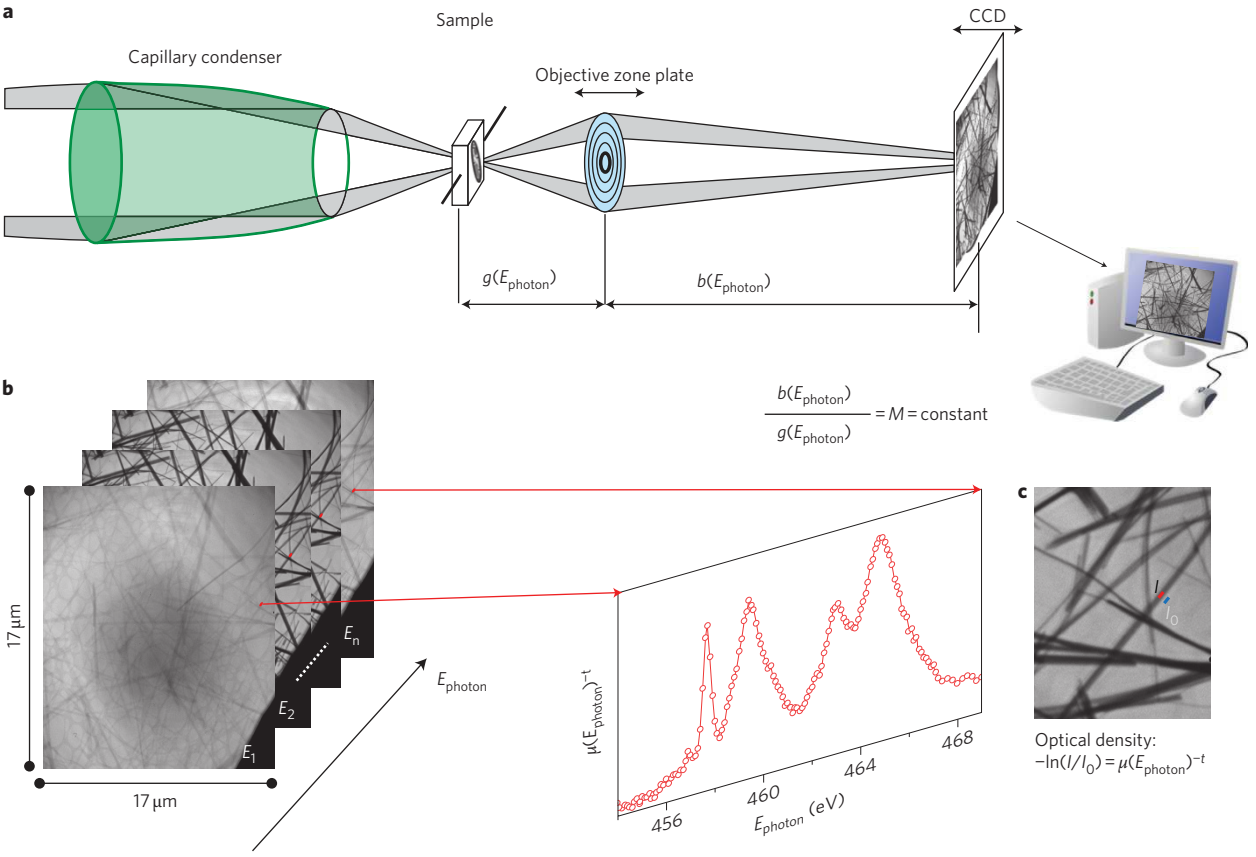

Figure 1 | Workflow for NEXAFS-TXM measurements. a, X-ray optical set-up of the TXM for NEXAFS studies. Monochromatized radiation from the undulator is focused by a reflective capillary condenser into the object field. A zone plate objective forms a magnified image. By choosing regions of interest (ROIs), the optical density can be calculated for each ROI using the sample-free region in its vicinity. As many nanostructures are within the field of view, one photon energy stack contains statistical information. **b**, Stack of (Na,H)TiNR images recorded at different energies. The NEXAFS spectrum is recorded on a ROI (shown in **c**). **c**, Schema showing a ROI for recoding the transmitted photon flux (I) and incident photon flux (I_0).

STXM. In practice, the high energy resolution provided by the monochromator can routinely be used without compromise for an exceptionally long exposure time. The workflow for NEXAFS-TXM measurements is shown in Fig. 1. Compared to EELS, the use of X-rays rather than electrons, as well as the relatively low irradiation dose per unit area associated with X-ray imaging, makes this technique well adapted for NEXAFS studies of electron-beam-sensitive materials such as biomaterials, polymers and nanostructures. Analysis of thicker samples (up to ~10 µm) is also possible.

The potential of NEXAFS-TXM for studying the electronic properties of individual anisotropic nanostructures was evaluated by analysing crystalline sodium titanate nanoribbons [(Na,H)TiNRs][16]. In the near-edge X-ray absorption fine structure method, the titanium L-absorption edge spectrum is very sensitive to the bonding environment, providing diagnostic information about the crystal structure and oxidation state[17]. The interest in titanate nanostuctures arises from their prospective use as active materials in applications such as lithium ion batteries, photocatalysts and dye-synthesized solar cells[18–21].

Figure 2a presents a TXM image of the (Na,H)TiNR sample recorded at a photon energy of 460 eV. In this image, a large number of nanostructures can be analysed individually, thus removing uncertainties relating to size variations of the nanostructures or the presence of impurities. In the following analysis, all data were obtained from the image stack, which also contains the image shown in Fig. 2a, and no further signal correction (including background subtraction) was applied to the spectra. To identify the spectroscopic fingerprints, we first analysed small nanoribbon bundles and compared the results with data recorded on standard powder samples that show a random orientation relative to the E-vector (Fig. 3). We also investigated the homogeneity of the nanoribbons and the linear dichroic characteristics of isolated nanostructures.

The titanium L-edge NEXAFS spectra from 15 different bundles of (Na,H)TiNRs share common general features with the spectra of rutile and anatase in that they are composed of distinguishable peaks in the range 455–470 eV corresponding to excitations of the Ti 2p states into the empty Ti 3d states (Fig. 3)[22]. All peaks are assigned to the TiO_6 octahedral environment; the titanium L-edge shows two groups of peaks arising from the spin–orbit splitting of the Ti 2p core level into $2p_{1/2}$ (L_2-edge) and $2p_{3/2}$ levels (L_3-edge). In TiO_2, the Ti 3d band is split into two sublevels with t_{2g} and e_g symmetry[23]. At photon energies below the L_3-edge, the low-intensity pre-peaks were reported to originate from particle–hole coupling[17,24]. The most prominent difference between these spectra is the fine structure of the L_3–e_g band. Using the multi-channel scattering (MCMS) method, Krüger showed that the L_3–e_g peak splitting in TiO_2 is due to structural differences beyond the first nearest-neighbour shell rather than distortion of individual octahedra[17,24,25]. In our spectra, the titanium L-peaks for the (Na,H)TiNR nanoribbons do not exactly align with those of any individual reference material, suggesting different charge distributions around the titanium atoms.

To better understand the absence of splitting in the L_3–e_g band, we removed the effect of the random orientation of the ribbons

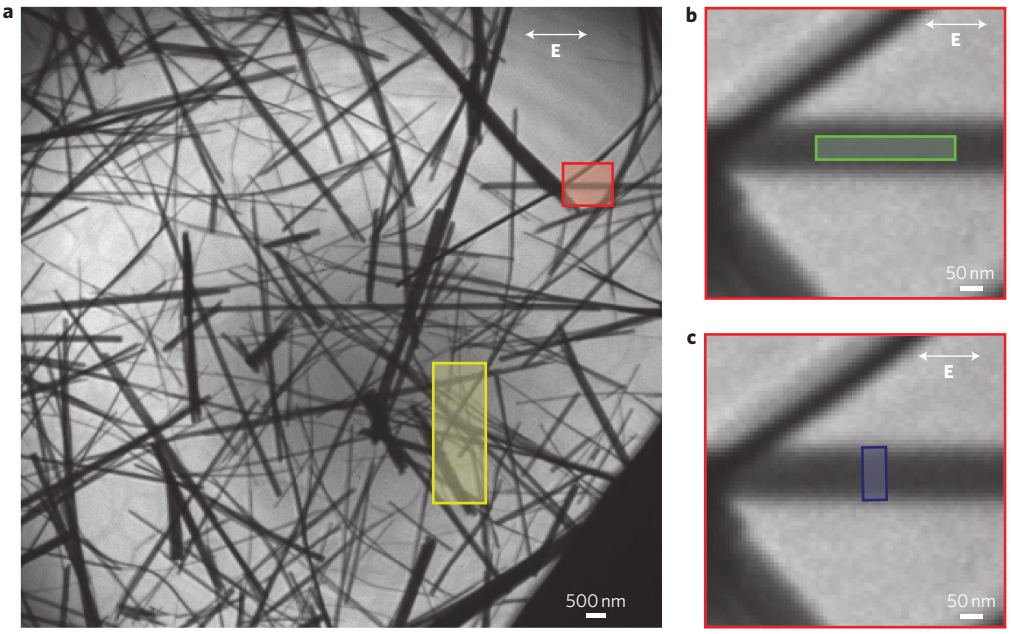

Figure 2 | Selected nanoribbons for data analysis. a, TXM micrograph of a (Na,H)TiNR sample imaged at $E = 460$ eV. The orientation of the electric field vector is indicated. The yellow rectangle shows a selected bundle of nanoribbons, the red square a selected ribbon. **b**,**c**, Region used for analysis of the selected nanoribbon (red box in **a**), with the rectangular area mainly parallel (**b**, green) and perpendicular (**c**, blue) to the principal axis of the ribbon.

relative to the electric field vector of the X-ray beam by examining the titanium *L*-edge spectra of isolated (Na,H)TiNR nanoribbons. First, titanium *L*-edge spectra were recorded in rectangular areas either parallel or perpendicular to the axis of the same ribbon, and were normalized to the intensity of the background signal (Fig. 4a). The L_3–t_{2g} spectra were found to be similar, whereas differences can be observed in the profile of the L_3–e_g peak and in the intensity of the L_2-band. In a second experimental geometry, titanium *L*-edge spectra were chosen for two different orientations of the E-vector, perpendicular and parallel to the principal axis of the selected ribbon (Fig. 4b, Supplementary Fig. S2). Comparing these spectra, we can observe the absence of splitting in the L_3–e_g band in both orientations. However, several features are shifted and broadened in the spectrum with the E-vector perpendicular to the principal axis of the ribbon, notably the e_g band, and the pre-peaks are more intense. Therefore, the absence of splitting of the L_3–e_g band in the spectrum of the (Na,H)TiNRs (Fig. 2) cannot be an artefact of their random orientation relative to the orientation of the E-vector, but must be an intrinsic characteristic of each individual sodium titanate nanoribbon. Andrusenko *et al.* reported that these nanoribbons are built from rigid layers of titanate octahedra interconnected by relatively weak Coulomb interactions via intercalated Na^+ cations and water molecules of crystallization[26]. These weakly bound species, especially those located near the edges, easily dislocate, causing shifts in the layers, that is, a localized deviation of the stacking vector[26,27]. The differences between the spectra in Fig. 4a can therefore be associated with different stacking orientations of the octahedra perpendicular or parallel to the principal axis of the selected ribbon. These results suggest that the absence of observed splitting of the e_g states is due to averaging over multiple types of titanium octahedral sites in the nanoribbons, in agreement with reports on the long-range structural character of the origin of the L_3–e_g peak splitting in TiO_2. Earlier studies have confirmed that, unlike in bulk reference TiO_2 samples, the nanoribbons contain significant quantities of H_2O/OH groups between the titanate layers that build hydrogen bonds to neighbouring octahedral structures of the ribbon, also distorting their shape[16]. The broadening observed when substituting Na^+ by protonation is due to the Coulombic interlayer interactions being supplemented by stronger directional hydrogen bonding, further increasing localized distortions of the titanium octahedra. This effect can be seen in the *L*-edge recorded on a bundle of protonated titanate nanoribbons [HTiNRs], which has broader

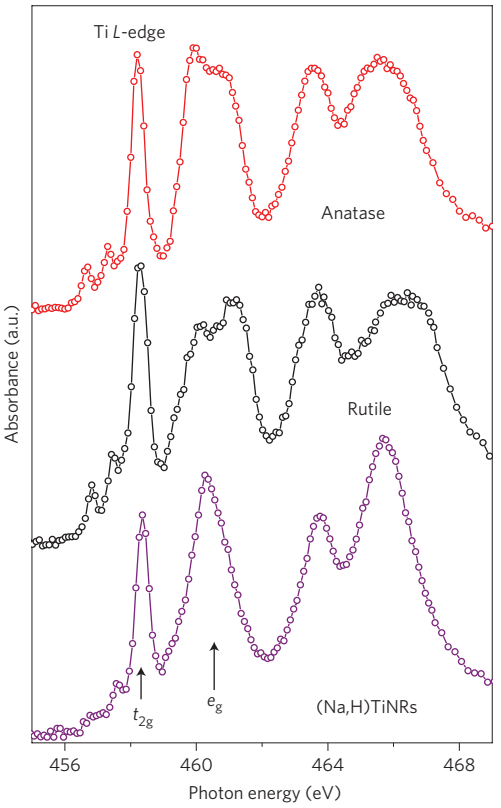

Figure 3 | Titanium *L*-edges recorded on anatase and rutile reference powder samples. Titanium *L*-edge spectra of the (Na,H)TiNRs are recorded on a bundle of nanoribbons with random orientation relative to the E-vector.

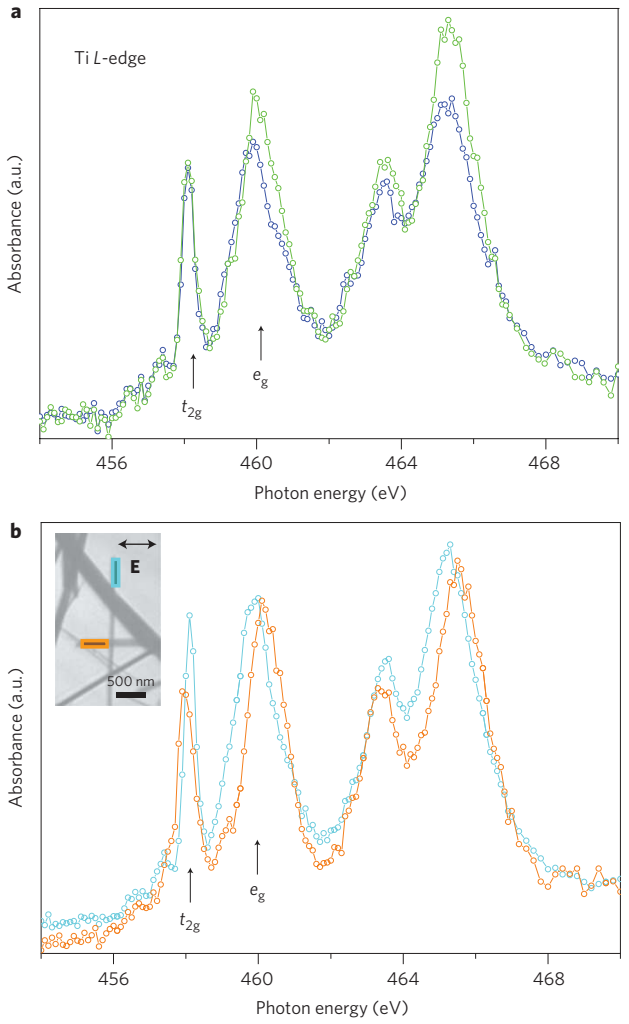

Figure 4 | Titanium *L*-edge spectra. a, Spectra recorded in a rectangular area perpendicular (blue) to the main axis of the (Na,H)TiNR (most of the octahedra are perpendicular to the principal axis of the ribbon) and parallel (green) to the principal axis of the ribbon (most of the octahedra are parallel to the principal axis of the ribbon). The applied geometry is shown in Fig. 2b,c. **b**, Spectra recorded on an isolated (Na,H)TiNR. The spectra were recorded in two experimental geometries: with the E-vector parallel (orange) or perpendicular (cyan) to the principal axis of the nanostructure (inset).

features than the *L*-edge recorded on a bundle of (Na,H)TiNR (Supplementary Fig. S3).

In summary, we show that the TXM is now capable of providing high-quality NEXAFS spectra with short exposure times and nanoscale resolution. This is demonstrated with NEXAFS spectra for individual (Na,H)TiNRs in different orientations of the nanoribbons relative to the electric field vector of the X-rays. The observed subtle variations in spectral absorption suggest that the absence of splitting of the e_g states in the (Na,H)TiNRs spectra is related to multiple stacking of a distorted TiO_6 octahedral structure. State-of-the-art TXM experiments routinely allow 25 nm (half pitch) spatial resolution[28]. Nevertheless, a higher spatial TXM resolution close to 10 nm has been reported recently[28], which will be available for spectromicroscopy applications in the near future. Because of its fast data collection and high penetration depth up to 10 μm, the NEXAFS-TXM method combined with nanotomography opens the way to study systems such as the interaction of nanostructures with biological cells, or complex organic hybrid nanomaterials. This study shows also the potential of NEXAFS-TXM for studying the interaction of nanostructures inside different matrices.

Methods

Materials. Sodium titanate nanoribbons ((Na,H)TiNRs) were synthesized from TiO_2 and NaOH(aq) under hydrothermal conditions at 175 °C. The detailed synthesis procedure is described in ref. 16. The influence of sodium within the NaTiO structure on the electronic structure was evaluated by studying protonated titanate nanoribbons (HTiNRs) prepared by ion-exchange with HCl acid solution from (Na,H)TiNRs (ref. 16). (Na,H)TiNRs (2 g) were washed three times in 200 ml of 0.1 M HCl and afterwards in distilled water. Elemental analyses were carried out using energy-dispersive X-ray spectroscopy: the sodium content in (Na,H)TiNRs was 7.2 wt%, but in HTiNRs was below 0.05 wt%.

Characterization. The morphology of the synthesized material was investigated with scanning (FE-SEM, Carl Zeiss, Supra 35LV) and transmission electron microscopes (TEM Jeol 2100, 200 keV). For TEM and NEXAFS-TXM analysis, the nanoribbons were sonically dispersed in ethanol and a drop of the solution was deposited onto a lacy carbon film supported by a copper grid. Note that because of electron-beam damage effects on the (Na,H)TiNR structure, the nanoribbons used for the electron microscopy analysis were not used for the TXM-NEXAFS analysis.

The (Na,H)TiNR sample was composed of elongated nanoribbons with diameters in the range of 20–200 nm (Supplementary Fig. S1)[29,30]. Some ribbons show bending contours indicating morphological distortion on the scale of the X-ray microscope resolution.

The NEXAFS-TXM Ti 2*p* *L*-edge spectra were recorded with the TXM installed at the undulator beamline U41-FSGM at BESSY II, Berlin. This provides a high spatial resolution close to 10 nm (half-pitch) and a spectral resolution up to $E/\Delta E \approx 1 \times 10^4$. In the full-field experimental configuration, the data of many isolated nanoribbons were simultaneously recorded and therefore already contained statistical information. Typical spectra are presented for each set of measurements. To verify the reproducibility of the results, 15 nanoribbons (with diameters varying from 70 to 180 nm) were analysed. The TXM allowed measurements to be taken at room or liquid-nitrogen temperatures in a vacuum of 1×10^{-7} torr. The spectra were recorded at room temperature in transmission mode by taking a sequence of images over a range of photon energies covering the investigated absorption edges with $E/\Delta E \geq 4{,}500$. Note that the exit slit of the monochromator was set to 5 μm, which corresponds to a calculated spectral resolution of $E/\Delta E = 2 \times 10^4$. The exposure time for one image with 1,340 × 1,300 pixels was typically 2–6 s. Taking an automated image stack with 230 images at different energies required ~90–120 min because of the time required for the necessary movements, camera readout and image storage.

The NEXAFS spectra were normalized, because the photon flux varies as a function of photon energy ($h\nu$) and time in the object field (x, y). Normalization was performed by dividing the function $I(x, y, h\nu)$ recorded on a single nanostructure by the photon flux curve $I_0(x + \Delta x, y + \Delta y, h\nu)$ recorded in a sample-free proximity at position $(x + \Delta x, y + \Delta y)$. Both $I(x, y, h\nu)$ and $I_0(x, y, h\nu)$ were recorded on the same image stack, because bare regions near each studied nanostructure allow the measurement of I_0.

The electronic structure of the nanoribbons is discussed in terms of the crystal field splitting with reference to micrometre-sized particles of anatase and rutile samples used as models for interpretation of the spectroscopic signatures. The TiO_2 polymorphs are titanium compounds with TiO_6 octahedral coordination. The stacked octahedra are distorted in the TiO_2 polymorphs (non-cubic ligand field).

References

1. Ade, H. & Hitchcock, A. P. NEXAFS microscopy and resonant scattering: composition and orientation probed in real and reciprocal space. *Polymer* **49,** 643–675 (2008).
2. Najafi, E. *et al.* Polarization dependence of the C 1*s* X-ray absorption spectra of individual multi-walled carbon nanotubes. *Small* **4,** 2279–2285 (2008).
3. Felten, A. *et al.* Individual multiwall carbon nanotubes spectroscopy by scanning transmission X-ray microscopy. *Nano Lett.* **7,** 2435–2440 (2007).
4. Sasaki, T. *et al.* Performance of low-voltage STEM/TEM with delta corrector and cold field emission gun. *J. Electron. Microsc.* **59,** S7–S13 (2010).
5. Suenaga, K. & Koshino, M. Atom-by-atom spectroscopy at graphene edge. *Nature* **468,** 1088–1090 (2010).
6. Krivanek, O. L. *et al.* High-energy-resolution monochromator for aberration-corrected scanning transmission electron microscopy/electron energy-loss spectroscopy. *Phil. Trans. R. Soc. A* **367,** 3683–3697 (2009).
7. Hitchcock, A. P., Dynes, J. J., Johansson, G., Wang, J. & Botton, G. Comparison of NEXAFS microscopy and TEM-EELS for studies of soft matter. *Micron* **39,** 311–319 (2008).
8. Stohr, J., Padmore, H. A., Anders, S., Stammler, T. & Scheinfein, M. R. Principles of X-ray magnetic dichroism spectromicroscopy. *Surf. Rev. Lett.* **5,** 1297–1308 (1998).

9. Smith, A. P. & Ade, H. Quantitative orientational analysis of a polymeric material (Kevlar® fibers) with X-ray microspectroscopy. *Appl. Phys. Lett.* **69,** 3833–3835 (1996).
10. Locatelli, A. & Bauer, E. Recent advances in chemical and magnetic imaging of surfaces and interfaces by XPEEM. *J. Phys. Condens. Matter* **20,** 093002 (2008).
11. Jacobsen, C., Wirick, S., Flynn, G. & Zimba, C. Soft X-ray spectroscopy from image sequences with sub-100 nm spatial resolution. *J. Microsc.* **197,** 173–184 (2000).
12. Krivanek, O. L. *et al.* Gentle STEM: ADF imaging and EELS at low primary energies. *Ultramicroscopy* **110,** 935–945 (2010).
13. Suenaga, K. *et al.* Visualizing and identifying single atoms using electron energy-loss spectroscopy with low accelerating voltage. *Nature Chem.* **1,** 415–418 (2009).
14. Schneider, G. Cryo X-ray microscopy with high spatial resolution in amplitude and phase contrast. *Ultramicroscopy* **75,** 85–104 (1998).
15. Schneider, G. *et al.* Three-dimensional cellular ultrastructure resolved by X-ray microscopy. *Nature Methods* **7,** 985–987 (2010).
16. Umek, P., Korosec, R. C., Jancar, B., Dominko, R. & Arcon, D. The influence of the reaction temperature on the morphology of sodium titanate 1D nanostructures and their thermal stability. *J. Nanosci. Nanotechnol.* **7,** 3502–3508 (2007).
17. Kruger, P. Multichannel multiple scattering calculation of $L_{2,3}$-edge spectra of TiO_2 and $SrTiO_3$: importance of multiplet coupling and band structure. *Phys. Rev. B* **81,** 125121 (2010).
18. Jamnik, J. *et al.* Stabilizers of particle size and morphology: a road towards high-rate performance insertion materials. *Adv. Mater.* **21,** 2715–2719 (2009).
19. Han, C. H. *et al.* Synthesis of Pd or Pt/titanate nanotube and its application to catalytic type hydrogen gas sensor. *Sens. Actuat. B* **128,** 320–325 (2007).
20. Baiju, K. V. *et al.* Correlating photoluminescence and photocatalytic activity of mixed-phase nanocrystalline titania. *Catal. Lett.* **130,** 130–136 (2009).
21. Qu, J., Gao, X. P., Li, G. R., Jiang, Q. W. & Yan, T. Y. Structure transformation and photoelectrochemical properties of TiO_2 nanomaterials calcined from titanate nanotubes. *J. Phys. Chem. C* **113,** 3359–3363 (2009).
22. Diebold, U. The surface science of titanium dioxide. *Surf. Sci. Rep.* **48,** 53–229 (2003).
23. Brydson, R. *et al.* Electron energy-loss spectroscopy (EELS) and the electronic-structure of titanium-dioxide. *Solid State Commun.* **64,** 609–612 (1987).
24. Degroot, F. M. F., Fuggle, J. C., Thole, B. T. & Sawatzky, G. A. $L_{2,3}$ X-ray-absorption edges of D^0 compounds—K^+, Ca^{2+}, Sc^{3+} and Ti^{4+} in O_h (octahedral) symmetry. *Phys. Rev. B* **41,** 928–937 (1990).
25. Crocombette, J. P. & Jollet, F. Ti 2*p* X-ray-absorption in titanium dioxides (TiO_2)—the influence of the cation site environment. *J. Phys. Condens. Matter* **6,** 10811–10821 (1994).
26. Andrusenko, I. *et al.* Structure analysis of titanate nanorods by automated electron diffraction tomography. *Acta Crystallogr. B* **67,** 218–225 (2011).
27. Umek, P. *et al.* Coordination of intercalated Cu^{2+} sites in copper doped sodium titanate nanotubes and nanoribbons. *J. Phys. Chem. C* **112,** 15311–15319 (2008).
28. Rehbein, S., Heim, S., Guttmann, P., Werner, S. & Schneider, G. Ultrahigh-resolution soft-X-ray microscopy with zone plates in high orders of diffraction. *Phys. Rev. Lett.* **103,** 110801 (2009).
29. Humar, M. *et al.* Mechanical properties of titania-derived nanoribbons. *Nanotechnology* **17,** 3869–3872 (2006).
30. Papa, A. L., Millot, N., Saviot, L., Chassagnon, R. & Heintz, O. Effect of reaction parameters on composition and morphology of titanate nanomaterials. *J. Phys. Chem. C* **113,** 12682–12689 (2009).

Acknowledgements

The authors thank S. Heim and R. Follath for their support during the development of the TXM and beamline. This work was funded in part by the Human Frontier Science Program (research grant RGP0053/2005-C), the German Federal Ministry of Education and Research (contract 05KS4BY1/7), the Helmholtz-Zentrum Berlin für Materialien und Energie GmbH, the Slovenian Research Agency (J2-9217), the COST Action MP0901, and the European Commission (contracts RII3-CT 2004-506008 (IASFS) and ERC 246791 (COUNTATOMS and ESMI)).

Author contributions

P.G. contributed to the design and construction of the microscope and collected all NEXAFS data sets. C.B. prepared all of the specimens, helped collect the X-ray data and performed the analysis of the NEXAFS data. S.R. designed and constructed the zone plate objectives and assisted with microscope construction. P.U. synthesized the nanostructures and, together with X.K., performed TEM and SEM analysis, G.V.T. and C.P.E., together with C.B., analysed the NEXAFS and electron microscopy data. G.S. had the idea for the new TXM, directed the X-ray microscopy project and designed and built the microscope with his colleagues. All authors read and contributed to the Article.

Additional information

The authors declare no competing financial interests. Supplementary information accompanies this paper at www.nature.com/naturephotonics. Reprints and permission information is available online at http://www.nature.com/reprints. Correspondence and requests for materials should be addressed to C.B. and G.S.